



Solvent Vapor Induced Film Formation of PS/AgNPs Composites Using Spectroscopic Techniques

Can Akaoglu and Şaziye Uğur*

Physics Engineering Department, Faculty of Science and Letters, İstanbul Technical University, 34469 Maslak, İstanbul, Turkey

Abstract: In this work, pyrene labeled polystyrene (PS) latex dispersions and silver nanoparticles (AgNPs) were mixed at different weight ratios of AgNPs in the range of 0-50 wt%. Powder (PS/AgNPs) films were prepared on glass substrates from these mixtures by the drop-casting method at room temperature. The fast transient fluorescence (FTRF) technique was used to monitor the film formation process of PS/AgNPs composites by measuring the fluorescence lifetimes of pyrene during vapor exposure. It was observed that pyrene lifetimes decreased as vapor exposure time, t increased obeying Stern–Volmer kinetic. The optical transmission (UVV) experiments showed that the transparency of the films decreased with increasing AgNPs content. Transparent films were produced for the composites with 0 to 20 wt % of AgNPs content. The Prager–Tirrel model was employed to FTRF and UVV data to obtain back-and-forth frequencies, ν , of the reptating PS chains during vapor induced film formation process and polymer interdiffusion was found to obey a $t^{1/2}$ law. Despite the conductivity increased by 3 orders of magnitude with increasing AgNPs content, the composites behaved like an insulator. The morphology of composite films also progressively changed during vapor exposure and affected by AgNPs content.

Received on 30-08-2018
 Accepted on 23-10-2018
 Published on 12-11-2018

Keywords: Polystyrene, Silver Nanoparticles, Films, Coatings, Solvent Vapor, Latex.

DOI: <https://doi.org/10.6000/2369-3355.2018.05.02.1>

INTRODUCTION

Latex materials are frequently used in modern industry [1,2]. Paints, paper coatings, and water-based adhesives are commonly referred to as applications of latex. Although synthetic latex is produced in large quantities and used in many applications, many aspects of its formation still remain unknown. Many factors are known to affect the final material properties. The most difficult topic in latex film formation study is the origin of the forces that cause a latex dispersion to evolve into a continuous film. Historically, the process of film formation has been divided into three or more stages [3,4]. Definitions of the stages differ among authors, although the generally accepted mechanism consists of: (i) evaporation from a stable dispersion which brings the particles into a close-packed form; (ii) deformation of particles, leading to a structure without voids, although with the original particles still distinguishable; (iii) interdiffusion of polymer chains across particle boundaries, yielding a continuous film with mechanical integrity and with the original particles no longer distinguishable.

Theoretical and experimental studies have made possible deep insights into the film formation process of latex particles

[4-8]. This knowledge is important to design high-performance coatings and develop new materials. In addition to the application of pure latex polymers as protective layers, polymer nanocomposites can be used for the coating industry. Composite materials form a class of materials in which immiscible compounds are combined in order to obtain new properties [9]. They are heterogeneous mixtures of their components which are generally of quite different properties. Their properties often depart very much from those of the pure components, so that mixing two homogeneous materials into a composite, results in the formation of a new material. Properties depend much more on the morphology and adhesion properties at the interfaces than on the volume and/or weight fraction of each phase as would happen in an ideal mixture. However, the film formation process of composite latex is more complicated than homogeneous one due to the interactions between the different phases. In addition, several factors such as molecular weight and its distribution, synthetic methodology, morphologies of latex particles, stabilizers, surfactants, annealing, film formation conditions, etc. were experimentally shown to influence composite latex film formation [10,11]. Within the past decades, there has been enhanced interest in using water based polymer latexes to create nanocomposites by filling polymers with inorganic natural and/or synthetic compounds [12]. Polymer nanocomposite shows unique properties,

*Physics Engineering Department, Faculty of Science and Letters, İstanbul Technical University, 34469 Maslak, İstanbul, Turkey; Tel: +90 212 285 66 03; Fax: +90 2122 85 63 86; E-mail: saziye@itu.edu.tr

combining the advantages of the inorganic nanofillers (such as rigidity, thermal stability) and the organic polymers (such as flexibility, dielectric, and processability) [13]. A defining feature of polymer nanocomposites is that the small size of the fillers leads to a dramatic increase in the interfacial area as compared with traditional composites. This interfacial area creates a significant volume (or weight) fraction of interfacial polymer with properties different from the bulk polymer even at low loadings [14]. Inorganic nanoscale building blocks [15,16] include metals (e.g. Ag, Fe, Ge), semiconductors (e.g. PbS, ZnO), clay minerals (e.g. montmorillonite, saponite), metal oxides (e.g. TiO₂, Al₂O₃), and carbon-based materials (e.g. carbon nanotube, graphite, carbon nanofiber) and so forth. The choice of polymer matrix is also manifold depending on the applications that can be generally divided into industrial plastics (e.g. polyimide, polypropylene), conducting polymers (e.g. polypyrrole, polyaniline), and transparent polymers (e.g. PMMA, PS).

Since traditional conductors based on metals are not intrinsically stretchable, various fabrication methods have been employed to make stretchable conductors based on composite materials due to their straightforward and low cost fabrication processes [17]. The combination of metal nanoparticles in the polymer matrix has gained sustained research interest as their fine control of size and shape leads to the fabrication of materials with novel electronic, magnetic and catalytic properties. This offers some level of controllable performance. Nanostructuring the polymer-metal interface in thin films demonstrates curial for organic photovoltaics, flexible electronics, and sensors [18]. However, they still present limitations in mechanical flexibility and electrical durability following the damage caused during their lifetime. For stretchable and flexible electronics, there is a great demand for elastomeric and conductive materials that show sufficient conductivity at large strains and display healing properties which improve the device's lifetime [19,20]. Conventionally, the polymerization of monomers and formation of metal particles are performed separately, and then the polymer and metal particles are mechanically mixed to form composites. The thermal annealing as well can artificially modify the morphology of embedded metal nanoparticles. However, it is difficult to disperse the metal particles homogeneously into the polymer matrix due to the easy agglomeration of the metal particles and the high viscosity of the polymer [19,20]. Organic solvent vapor is an effective means to generate order in polymer systems. When solvent enters a film, the resultant plasticization drastically increases the mobility of the polymer chains. When exposed to a solvent vapor these conducting composites exhibit good sensitivity through a drastic increase in their resistance. Because, the organic solvent vapor promotes the solubilization and crystallization of the filler, plastication of the polymer chains, and migration of the filler.

The thin film of polymeric composites obtained spinning a carbon black/thermoplastic polymer dispersion have already

shown their potentialities as basic elements of commercial electronic noses [21]. The hypothesis generally used in order to describe qualitatively the working mechanism of these sensors considers that polymer matrix swells when exposed to organic vapor and the swelling decreases the connectivity between the conductive filler particles [21]. Recently, Cui *et al.* [22] studied self-healing property of PDMS-containing urea segmented copolymer. The mechanically bisected polymer showed healing efficiency of 50%, where healing is thought to have occurred through disassembly and assembly of the polymer network at the surfaces of the damaged site when brought together. They showed that the self-healing required high temperatures above 50°C or a long time, at least 2 weeks, at room temperature. On the other hand, Wilson, *et al.* [23], proposed a more efficient method for crack repair of thermoplastics exposing the elastomer to an organic solvent. Using this method, they promoted the healing process of thermoplastics through the entanglement of the polymer chains by lowering the glass transition temperature below room temperature [24]. Baek *et al.*, studied the electrical conductivity, mechanical and solvent vapour-induced self-healing properties of composites with various weight fractions of FeCl₃-doped P3HT [25]. A freestanding film with 30 wt % of doped P3HT was further examined for self-healing under a solvent vapor, and the recovery of the electrical and mechanical properties was evaluated. They found that 30min of solvent vapour exposure led to mechanical healing efficiency of 55% and recovery of 82% of its conductivity.

Pyrene (P) chromophore [26] is an attractive choice for studying dynamics in polymers. The long excited singlet lifetime of pyrene [26] makes it an attractive choice for studying dynamics in polymers. Simple alkyl P derivatives fluoresce intensely at wavelengths of 370-450nm. P has been successfully employed as a fluorescence probe in the study of micellar [27] and phospholipid dispersions [28]. These studies focus on the use of the dynamics of quenching of P monomer fluorescence and excimer formation process. The other application of P as a fluorescence probe is in the study of the vibronic fine structure of its monomer fluorescence. The intensities of the various vibronic bands show a strong dependence on the solvent environment [29]. In the presence of polar solvents there is an enhancement in the intensity of the 0-0 band, whereas there is little effect on the other bands; thus the ratio of intensities of these bands was used to study the environmental change. The transient fluorescence (TRF) technique for measuring fluorescence decay has been routinely applied to study many polymeric systems using dyes as a probe and/or as labels [30,31]. TRF spectroscopy with direct energy transfer (DET) and quenching method has been used to characterize the internal morphologies of composite polymeric materials [32]. A single-photon counting (SPC) technique, which produces decay curves and measures lifetimes of conjunction with DET, was used to study the diffusion of small dye molecules within the interphase domain of anthracene- and/or phenanthrene-labeled poly(methyl methacrylate) (PMMA) particles [33]. The

mean lifetimes of donor dye molecules that exhibit fluorescence were measured during diffusion. A Fickian model [34] for diffusion was employed to produce diffusion coefficients.

Understanding the nature of the interfacial region between an organic polymer matrix and an inorganic filler component is essential in determining how this region impacts the overall bulk properties of the composite material. Up to now, much research has been carried out to gain an understanding of these effects. However, despite these efforts, the research remains incomplete and requires further exploration and investigation. Here, we present a simple route to prepare composite films that can address some of these issues through solvent vapor-induced film formation. We prepared powder PS/AgNPs composite films with different AgNPs content using the drop-casting method at stage (ii). Then film samples were exposed to solvent vapor to provide in-depth insight into how the AgNPs content affect the film formation, morphological and electrical properties of PS/AgNPs films. Film formation process was observed by monitoring the excited-state decay curves at 375 nm and transmitted light intensity, I_{tr} at 600 nm. P lifetimes were measured using the strobe technique, which is referred to as FTRF. The major advantage of the strobe technique over others is the duration of a single experiment, which takes only a few seconds. Chloroform–heptane mixture was used as plasticizer and in situ FTRF experiments were performed to observe the film formation process. Experiments were carried out by illuminating the film samples and fluorescence decay traces were observed using the Strobe Master System (SMS). As a supporting experiment, the real-time monitoring of the transmitted light intensity, I_{tr} , through the films were also performed during film formation. The decrease in pyrene lifetime, $\langle \tau \rangle$, and the increase in I_{tr} with respect to solvent induction time were attributed to the increase in “crossing density” at the polymer-polymer interface. Back and forth frequencies, ν , of the reptating PS chains were measured and found to be substantially affected with AgNPs content in the composite film.

THEORETICAL CONSIDERATIONS

Fluorescence Quenching

Emission of fluorescence is a radiative transition of an electronically excited molecule from its singlet excited state to its ground state [35]. When an organic dye absorbs light, it becomes electronically excited; then fluorescence occurs from the lowest excited singlet state and decays over a time scale of typically nanoseconds [35]. In addition to unimolecular decay pathways for deexcitation of excited states, a variety of bimolecular interactions can lead to deactivation. These are referred to collectively as quenching processes, which enhance the rate of decay of an excited state intensity, I , as

$$I = A \exp\left(-\frac{t}{\tau}\right) \quad (1)$$

where A is the pre-exponential factor and τ is the lifetime that characterizes the time scale of excited state decay.

Fluorescence quenching normally refers to any bimolecular process between the excited singlet state of a fluorescence dye and a second species that enhances the decay rate of the excited state. One can schematically represent the process as



where F and F^* represent the fluorescent molecule and its excited form, and Q is the quencher. k_f , k_{nr} , and k_q represent the fluorescence, nonradiative, and quenching rate constants, respectively. Kinetically, quenching processes can be divided into two main categories: dynamic and static (which is not of interest to us). Dynamic quenching is most likely to occur in fluid solution, where the dye or quencher is free to move. If the quenching rate can be characterized in terms of a single rate coefficient (k_q), the unquenched decay rate of F and a unique lifetime, τ_0 , then the quenching kinetics will follow the Stern–Volmer equation,

$$\tau^{-1} = \tau_0^{-1} + k_q [Q] \quad (4)$$

where $[Q]$ represents the quencher concentration.

Crossing Density

A homopolymer chain with N freely jointed segments of length L was considered by Prager-Tirrell (PT) [36], which moves back and forth by one segment with a frequency ν [37]. In time the chain displaces down the tube by a number of segments, m . Here, $\nu/2$ is called the ‘diffusion coefficient’ of m in one-dimensional motion. PT calculated the probability of the net displacement with m during the time t in the range of $m-\Delta$ to $m-(\Delta+d\Delta)$ segments. A Gaussian probability density was obtained for small times and large N . The total “crossing density” $\sigma(t)$ (chains per unit area) at junction surface then was calculated from the contributions $\sigma_1(t)$ due to chains still retaining some portion of their initial tubes, plus a remainder σ_2 i.e. contribution comes from chains which have relaxed at least once. σ_1 and σ_2 contributions to σ are presented in Figure 1 at the interface. In terms of reduced time $\tau = 2\nu t / N^2$ the total crossing density can be written as

$$\sigma(\tau) / \sigma(\infty) = 2\pi^{-1/2} \times \left[\tau^{1/2} + 2 \sum_{k=0}^{\infty} (-1)^k \left[\tau^{1/2} \times \exp(-k^2 / \tau) - \pi^{-1/2} \times \operatorname{erfc}(k / \tau^{1/2}) \right] \right] \quad (5)$$

where n and k are the running indexes of the series. For small τ values, the summation term can be neglected, which then results in [36,38]

$$\sigma(\tau) / \sigma(\infty) = 2\pi^{-1/2} \tau^{1/2} \quad (6)$$

This was predicted by de Gennes [37] on the basis of scaling arguments.

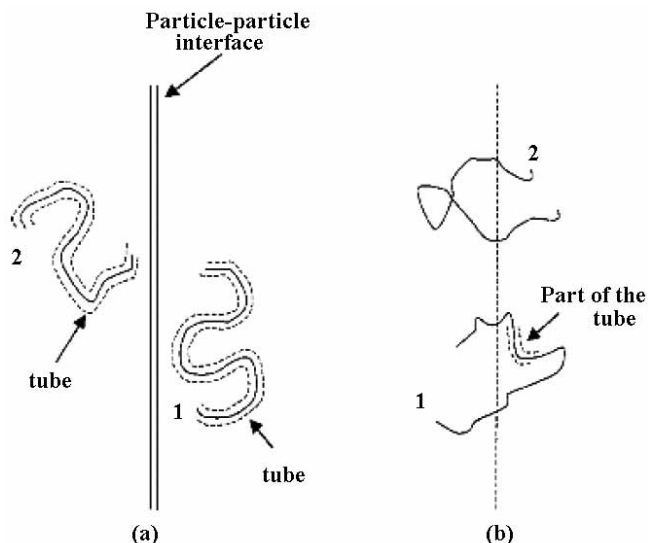


Figure 1: Schematic representation of a reptating polymer chain at the particle–particle interface. 1 and 2 represent the σ_1 and σ_2 contributions to the total crossing density, σ .

EXPERIMENTAL SECTION

Materials

Fluorescent polystyrene (PS) latexes were produced via an emulsion polymerization process [39]. The polymerization was performed batchwise using a thermostated reactor equipped with a condenser, thermocouple, mechanical stirring paddle, and nitrogen inlet. Water (50ml), styrene monomer (3g; 99% pure from Janssen), and 0.014g of fluorescent 1-pyrenyl methyl methacrylate (PolyFluor® 394) were first mixed in the polymerization reactor, where the temperature was kept constant (at 70°C). The water-soluble

radical initiator potassium persulfate (KPS) (1.6% wt/wt over styrene) dissolved in a small amount of water (2 ml) was then introduced in order to induce styrene polymerization. The surfactant sodium dodecyl sulfate (SDS) (0.025% wt/vol) were added to the polymerization recipe. The polymerization was conducted under agitation at 400rpm for 12h under a nitrogen atmosphere at 70°C. The particle size was measured using a Malvern Instruments (Malvern, UK) Nano ZS and the mean diameter of these particles was found to be 349nm. Figure 2a shows the SEM image of PS latex produced for this study. The weight-average molecular weights (M_w) of individual PS chains were measured by gel permeation chromatography (GPC) and found to be 2.66×10^5 g/mol. The glass transition temperatures (T_g) of the PS latexes were determined using a differential scanning calorimeter (DSC) and found to be around 105 °C.

Poly(vinyl pyrrolidone) (PVP) covered core-shell silver nanoparticles (AgNPs) of 95% purity (metal basis) were purchased from the SkySpring Nanomaterials, Inc. (Westhollow Dr, Houston, USA), in the powder form. These particles are composed of 25 wt% of Ag in the core and 75 wt% of PVP polymer in the shell and the average diameter of AgNPs is 15 nm. Figure 2b shows the SEM image of AgNPs used in this study.

Preparation of PS/AgNPs Nanocomposite Films

Composite film preparation was carried out in the following manner: A stock solution of PS particles was prepared by diluting PS dispersion with DI water (10.1g/L) under mechanical stirring. The seven different PS latex/AgNPs dispersions were prepared by adding a different amount of powder of AgNPs to PS latex dispersion. Further, these dispersions were magnetically stirred at least for 1h. Glass substrates which are 1 mm thick and $0.8 \times 2.5 \text{cm}^2$ in size were washed in acetone and deionized water, then dried in an oven. Each PS/AgNPs dispersion was subsequently coated onto the surface of the glass substrates by drop

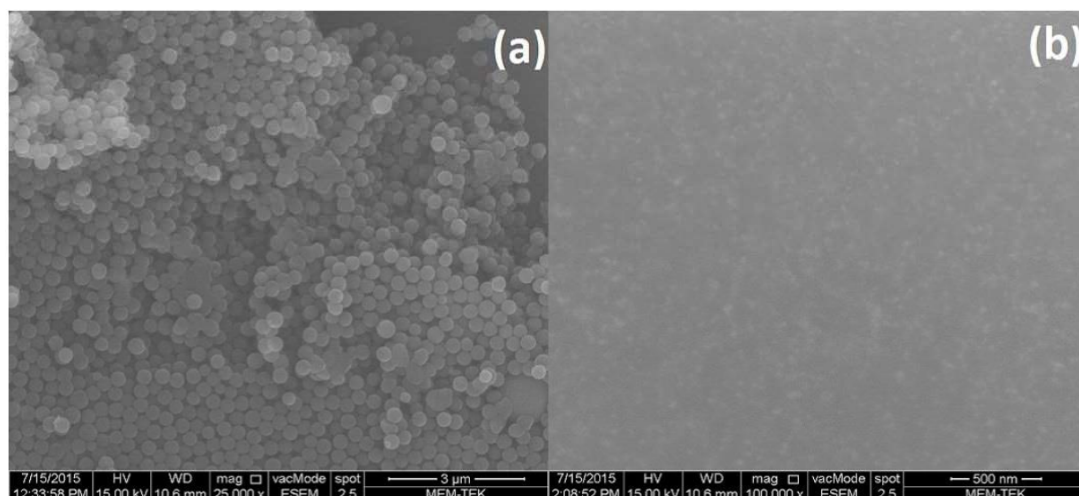


Figure 2: SEM images of (a) PS latex and (b) AgNPs used in this study.

casting method and dried at the room temperature. After drying process, seven different PS/AgNPs powder films with 0, 1, 5, 10, 20, 30 and 50 wt% of AgNPs content were obtained. Film samples were weighted before and after the film casting to determine the film thickness. The thickness of the films was determined from the weight and the density of samples ($\rho_{Ag}=10.49\text{g}\cdot\text{cm}^{-3}$, $\rho_{PVP}=1.2\text{g}\cdot\text{cm}^{-3}$ and $\rho_{PS}=1.05\text{g}\cdot\text{cm}^{-3}$) [40,41] and found to increase with increasing AgNPs content (see Table 1).

Measurement Methods

Fluorescence Decay Measurements

In situ fluorescence decay experiments were performed using Photon Technology International's (PTI) SMS. In the strobe, or pulse sampling, technique [42] the sample was excited with a pulsed light source. The name is derived from the fact that the photomultiplier tube (PMT) is gated or strobed by a voltage pulse that is synchronized with the pulsed light source. The intensity of fluorescence emission is measured in a very narrow time window on each pulse and saved in a computer. The time window is moved after each pulse. The strobe has the effect of turning off the PMT and measuring the emission intensity over a very short time window. When the data were sampled over the appropriate range of time, a decay curve of fluorescence intensity versus time could be constructed. All the decay measurements were made at 90° position and slit widths were kept at 15nm. Experiments were performed in a 1x1-cm² quartz cell, which was placed in the SMS, and fluorescence decay was collected over three

decades of decay. Samples were placed in a quartz cell as it is shown in Figure 3 (position 1) with a solvent mixture composed of chloroform (as a good solvent for PS) and heptane (as a poor solvent for PS) at the bottom and then illuminated with 345-nm-excitation light; P fluorescence emission was detected at 375 nm. The uniqueness of the fit of the data to the model is determined by χ^2 ($\chi^2 < 1.20$), the distribution of weighted residuals, and the autocorrelation of the residuals. Seven different vapor-induced film formation experiments were run for the various AgNPs content.

Optical Transmission Measurements

Optical transmission experiments were carried out using Variant Carry-100 Bio UVVisible (UVV) scanning spectrometer. The transmittances of the films were detected at 600nm. The sample position and the transmitted light intensity, I_{tr} , are presented in Figure 3 (position 2). All measurements were made at the room temperature.

Scanning Electron Microscopy (SEM) Measurements

Scanning electron micrographs (SEM) of the PS/AgNPs films were taken at 15 kV in a JEOL 6335F microscope. A thin film of gold (10nm) was sputtered onto the surface of samples using a Hummer-600 sputtering system to help image the composite films against the glass background.

Electrical Conductivity Measurements

The Electrical conductivity measurements of the composite films were conducted with a Keithley 6517a Electrometer with an ultrahigh resistance meter using a two-probe method. For

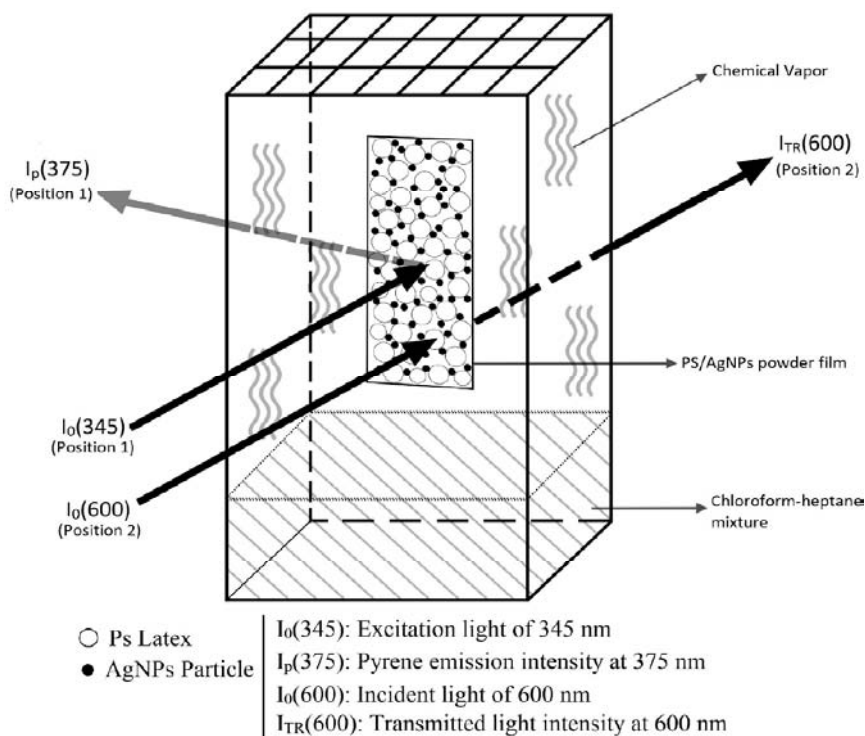


Figure 3: The position and the illumination of the composite film sample exposed to solvent vapor are shown in SMS (position 1) and UVV (position 2) systems. $I_0(345)$, $I_p(375)$, $I_0(600)$, and $I_{tr}(600)$ are the excitation, pyrene, incident and transmitted light intensities, respectively.

the surface resistance measurements, the samples were coated onto thin rectangular glass slabs with typical dimensions of $2.5 \times 2.5 \text{ cm}^2$. The electrical contact was made using a silver paste. Electrical resistivities of the composite films were measured by alternating polarity technique with electrometer and a test fixture. The composite films were placed in the test fixture, which have disk shaped electrodes, then their surface resistivities, $R_s (\Omega)$, were measured for 15 s under 100 V alternating potential. All the resistivities of the composite films were determined for four different

orientations and average of these measurements was taken for each film to lower the error level. The surface resistivity was converted into surface conductivity (σ) using the relation $\sigma = 1/R_s (\Omega)$.

RESULTS AND DISCUSSION

Mean Lifetimes

Figure 4 presents the fluorescence decay profiles of P in pure latex film at various film formation steps. It is observed that as

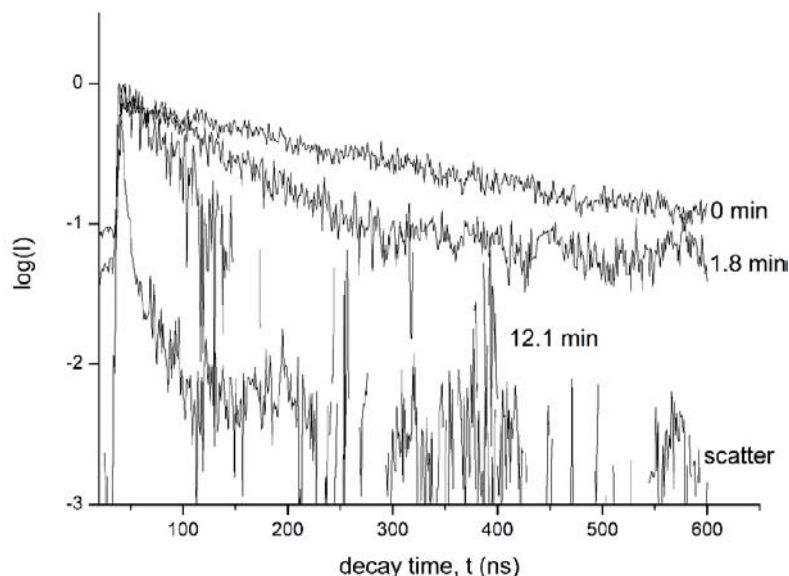


Figure 4: Fluorescence decay profiles of P from pure PS film at various film formation steps. The number on each curve represents the vapor exposure time, t , in minutes. The sharp peaked curve is the lamp profile.

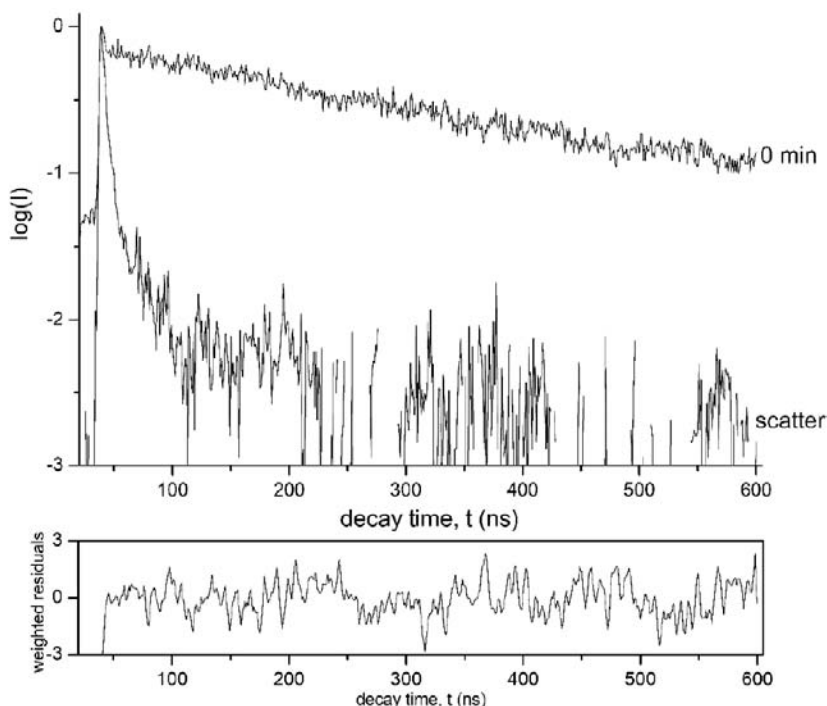


Figure 5: Typical fluorescence decay curve and its fit to Eq. (6), from which τ values are determined.

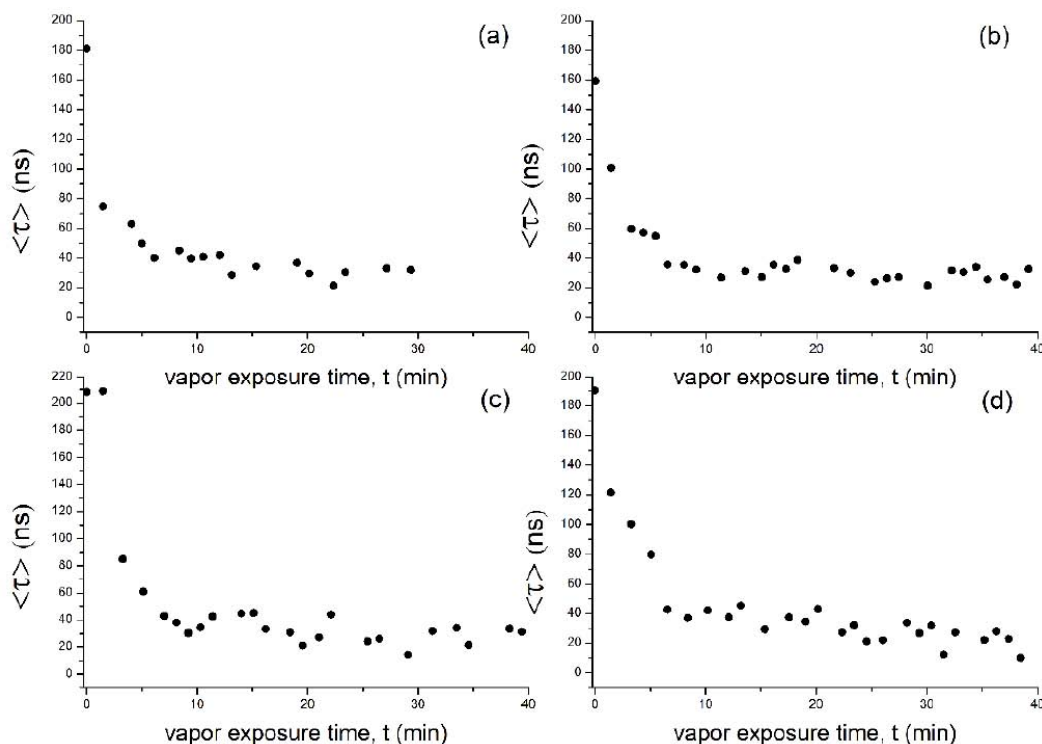


Figure 6: Plots of $\langle \tau \rangle$ values versus vapor exposure time, t , for the composite films with (a) 0, (b) 10, (c) 30 and (d) 50 wt% of AgNPs content.

the vapor exposure time, t is increased, excited P decay faster, indicating that the quenching of excited P increases. In order to probe the vapor-induced film formation processes, the fluorescence decay curves were measured and fitted to the sum of two exponential:

$$I = A_1 \exp\left(-\frac{t}{\tau_1}\right) + A_2 \exp\left(-\frac{t}{\tau_2}\right) \quad (7)$$

where t represents the decay time, τ_1 and τ_2 are the long and short components of P lifetimes, and A_1 and A_2 are the corresponding amplitudes of the decay curves. A typical decay curve and its fit to Eq. (7) is shown in Figure 5. (A_1, A_2) and (τ_1, τ_2) values were produced at each film formation step using the non-linear least squares analysis.

Mean lifetimes of P were calculated from the relation

$$\langle \tau \rangle = \frac{A_1 \tau_1^2 + A_2 \tau_2^2}{A_1 \tau_1 + A_2 \tau_2} \quad (8)$$

Using (A_1, A_2) and (τ_1, τ_2) values for the film formation experiments, $\langle \tau \rangle$ values are measured and plotted in Figure 6 versus solvent exposure time (t) for various AgNPs contents. It is observed that $\langle \tau \rangle$ values for all film samples decrease exponentially as t is increased. In order to understand the effect of AgNPs content on the quenching of excited P molecules, $\langle \tau \rangle$ values were also plotted as a function of AgNPs content in Figure 7 for various solvent exposure times. From these figures, it is seen that $\langle \tau \rangle$ values show no substantial change with varying AgNPs

content and the quenching process is mostly originated from the solvent molecules.

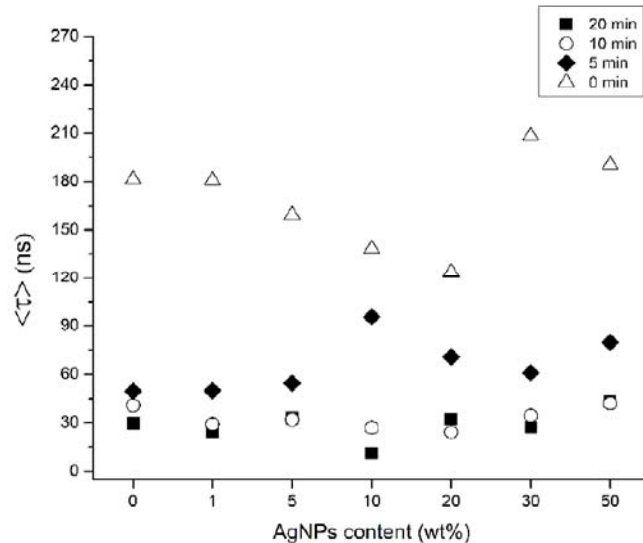


Figure 7: Plot of $\langle \tau \rangle$ values as as function of AgNPs content at various vapor exposure times of.

To quantify these results, a Stern–Volmer type of quenching mechanism is proposed and Eq. (4) can be employed. For low quenching efficiency, $\tau_0 k_q [M] < 1$; Eq. (4) becomes

$$\tau \approx \tau_0 (1 - \tau_0 k_q [M]) \quad (9)$$

Here, since we assume that solvent molecules are responsible for the quenching process, $[M]$ represents the

quencher (vapor) concentration at time t . The relation between the lifetime of P and [M] in film can be obtained approximately using the volume integration of Eq. (9) and the relation

$$\frac{\langle \tau \rangle}{\langle \tau_0 \rangle} = 1 - C \frac{M}{M_\infty} \quad (10)$$

where $C = \tau_0 k_q M_\infty / V$. Here V is the volume of the film. The vapor sorption is calculated over the differential volume as

$$M = \int_0^d [M] dV \quad (11)$$

where dV is the differential volume in the film and the integration is performed from 0 to d , where d is the film thickness. M_∞ is the amount of vapor sorption at time infinity.

In order to compare our results with the crossing density of the PT model, we can re-write Eq. (6) as

$$\sigma(\tau) / \sigma(\infty) = Rt^{1/2} \quad (12)$$

where $R = (8\nu / \pi)^{1/2} N^{-1}$. Combining Eq. (11) with Eq. (12) and assuming that vapor penetration is proportional to the chain interdiffusion due to plasticization, i.e., the increase in vapor sorption causes the increase in crossing density, $\sigma(t)$, then the following relation can be produced

$$1 - \frac{\langle \tau \rangle}{\langle \tau_0 \rangle} = Bt^{1/2} \quad (13)$$

where $B = CR$, is obtained. Plots of the data in Figure 6 according to Eq. (13) are shown in Figure 8. Fits are nice, and support the PT model, where chain transport obeys the $t^{1/2}$ time dependence. The slopes of the linear relations in Figure 8 produce B values with the accuracy of R^2 close to 1.0 in which the only variable is the reptation frequency, ν . The other parameters in C and R are constant during film formation processes. The produced B values are given in Table 1 and also plotted versus AgNPs content in Figure 9. It is seen that as AgNPs content is increased, B values first decrease up to the critical 10 wt% of AgNPs content, then start to increase. In this figure, circles and squares are experimental data and lines are guides for the eyes. Most probably large B values are caused by high crossing densities due to fast reptation of polymer chains. In other word, film formation accelerates in these films as a result of high solvent vapor absorption due to plasticization effect. The decrease in B values for 0-10 wt% of AgNPs range can be explained by the reptation of polymer chains at lower frequencies during film formation processes, which result in low B values. Here one may argue that due to steric hindrance by the AgNPs particles, the interdiffusion of polymer chains across the junction is retarded. As a result, polymer chains reptate slower at the polymer/polymer

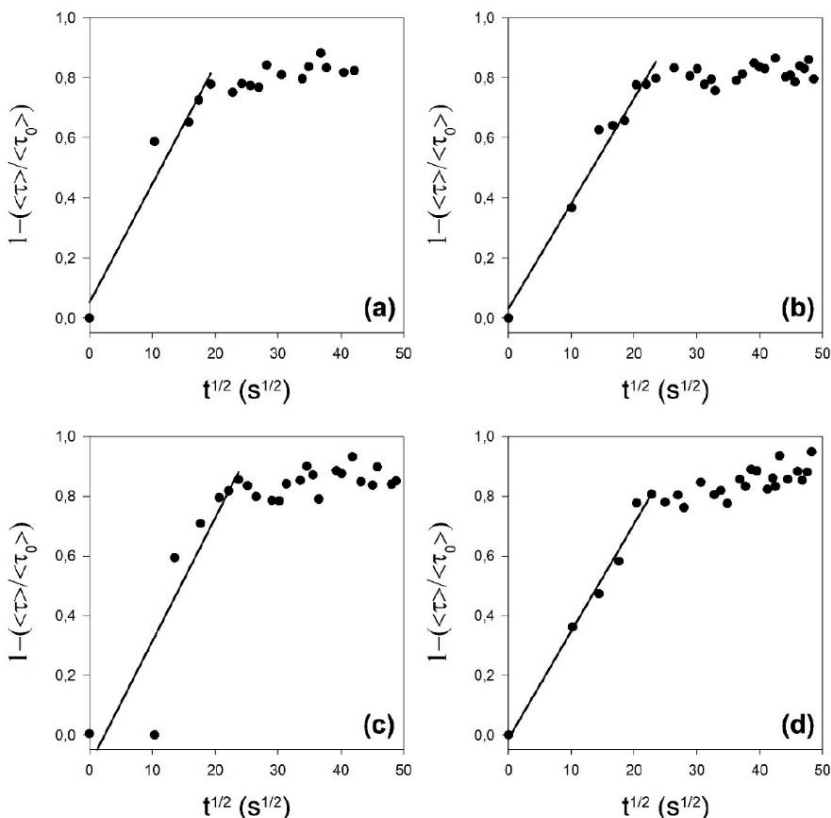


Figure 8: Plots of the data in Figure 6 according to Eq. (13), where linear least squares fits are performed. The slope of the linear relations produce B values.

interface, which results in low B values with increasing of AgNPs content from 0 to 10 wt%. The increase in B (or v) values above 10 wt% of AgNPs content can be explained by the formation of AgNPs aggregates which results in the formation of voids in the film (see Figure 14). Due to these voids, the solvent molecules diffuse faster into the composite films and enhance the reptation of PS chains.

Table 1: B (●), R (□) Values and Film Thicknesses of PS/AgNPs Composite Films Used in this Study

AgNPs (wt%)	B (s ^{-1/2})	R (s ^{-1/2})	d (μm)
0	0,040	0,161	5,3
1	0,040	0,083	12,1
5	0,035	0,118	10,3
10	0,028	0,106	9,1
20	0,032	0,139	10,4
30	0,041	0,157	19,2
50	0,036	0,251	25,2

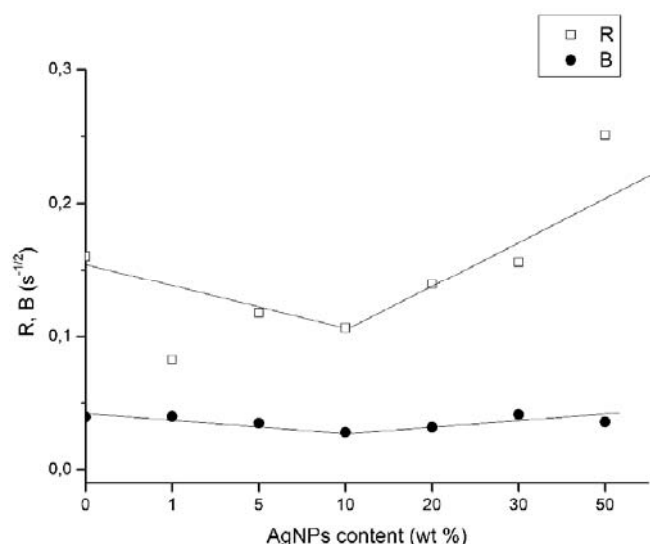


Figure 9: Plot of B (●) and R (□) values versus AgNPs content in the composite film.

Transmitted Light Intensities

In order to support above findings, transmitted light intensity (I_{tr}) data were obtained. Figure 10 presents I_{tr} versus time (t) plots for various AgNPs content. It can be seen that all curves increase as the vapor exposure time is increased and reach a plateau by suggesting that the composite films become more transparent to light. These behaviors can be explained with the chain interdiffusion between latex particles during vapor induced film formation. As the polymer chains interdiffuse, transparency of the film increases with time, which results in less light scattering from the composite film. This also indicates that vapor-induced film formation occurred in all film samples. Here it is interesting to note that all I_{tr} curves start

above 50% at 0 time, which may indicate that the diffusion of solvent vapor into films is too fast. Furthermore, as AgNPs content increased above 10 wt%, I_{tr} increases faster with solvent exposure time (t) by presenting smaller saturation values. Intuitively, this behaviour of I_{tr} predicts that film samples with high AgNPs content exposed to solvent vapor create the less transparent film in very short times. Beside this, it is worthy to note that I_{tr} curve of 50 wt% of AgNPs content film first increases reaching a maximum and then decreases with vapor exposure time. Since the solvent provides a medium for the solubilization of the AgNPs particles and at the same time plasticizes the polymer chains, it causes the migration and combination of AgNPs particles forming clusters (aggregates) at long vapor exposure time resulting strong scattering of the light. Therefore, the I_{tr} decreases with increasing vapor exposure time due to scattering of the light from these clusters.

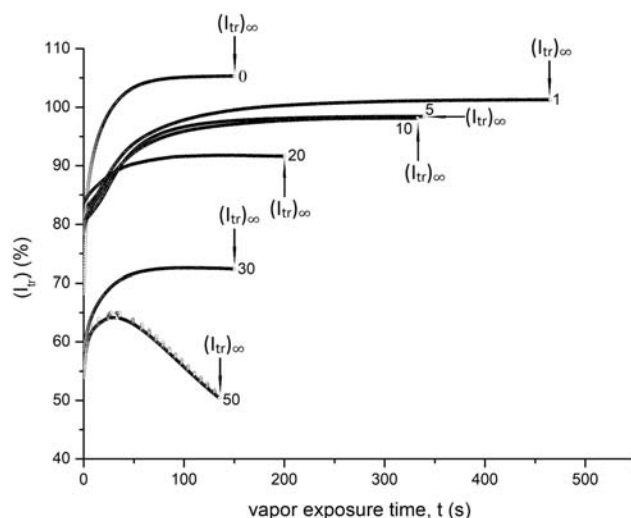


Figure 10: Plot of transmitted light intensities, I_{tr} , versus vapor exposure time, t, in seconds. The number on each curve indicates the AgNPs content in the film.

To make this point clear, the saturation values, $(I_{tr})_{\infty}$ of transmitted light intensity (I_{tr}) curves in Figure 10 were plotted versus AgNPs content in Figure 11. It is seen that as increasing the AgNPs content from 0 to 20 wt%, the transmittance of composite films decreased almost gradually from 105% to 92%. However, the transmittance decreased rapidly from 92% to 72% increasing AgNPs content from 20 to 30 wt% and then to 51% at 50 wt% of AgNPs. The composite films with transmissions above 85% correspond to transparent films, whereas films with transmission below 20% and in between them correspond to turbid and translucent films, respectively. In our case, the results indicate that transparent composite films (105%-92%) were successfully achieved for 0-20 wt% of AgNPs contents, but translucent films (72-51%) were obtained for 30-50 wt% of AgNPs contents. As it is known that the transparency of composite films depends mainly on three factors: differences in refractive indices, sizes of phases, and the number and size of air voids in the composite films [43,44]. Here, despite the

refractive indices of PS polymer ($n=1.59$) and AgNPs particles ($n_{\text{PVP}}=1.53$, $n_{\text{Ag}}=0.072$ and $n_{\text{AgNPs}}=1.17$) [45] are somewhat different (about 0.42), we suggest that the low I_{tr} for higher AgNPs content films is mostly associated with aggregation of AgNPs [46] in the films which can scatter the light. As argued above, due to the plastization effect of the solvent vapor, the voids are completely filled by the PS polymer during vapor induced film formation and almost no voids are present in the films. Therefore, optical transmission in these films can be qualitatively related to AgNPs clusters. Drawing upon the SEM results shown in the following section (see Figure 15), we can conclude that the clustering of AgNPs particles scatter light significantly, so that the optical transmission is reduced with increasing AgNPs content. As the size of AgNPs clusters is large with respect to the wavelength of the visible light, they scatter the light that causes low I_{tr} . Because of the continuous film formation of PS, transparency is high (>90%) for composite films with AgNPs content in the range of 0-20 wt%. As the AgNPs content is increased above 20 wt%, the transmission decreases dramatically (around 51%) which results in translucent films. Thus, it can be concluded that the AgNPs and the PS phases existed as two separate phases in these films as seen in SEM images in the following section.

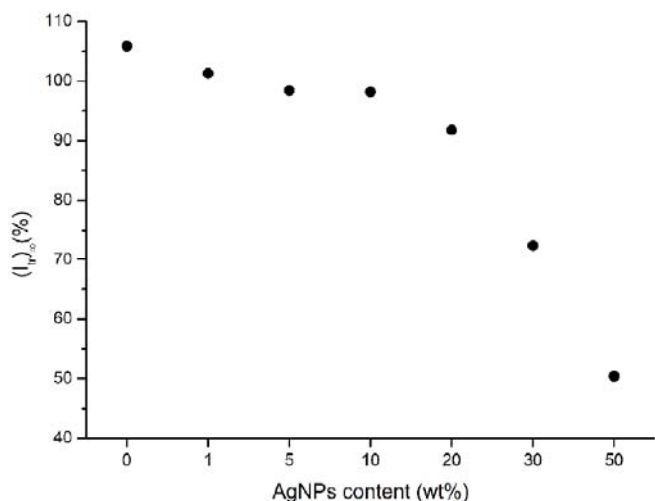


Figure 11: Plot of saturation values, ($I_{\text{tr}}\text{)}_{\infty}$ of I_{tr} curves as a function of AgNPs content.

To compare our results with Prager-Tirrel model, we assume that $I_{\text{tr}}(t)$ ($=[I_{\text{tr}}(t) - I_{\text{tr}}(0)]$) is proportional to the crossing density, $\alpha(t)$, in Eq.(6), then the following phenomenological equation can be written [35]:

$$\frac{I_{\text{tr}}(t)}{I_{\text{tr}}(t_{\infty})} = Rt^{1/2} \quad (14)$$

The above assumption requires the disappearance of particle-particle interfaces due to the chain interdiffusion which causes an increase in I_{tr} . The plots of Eq. (14) for the data in Figure 10 are shown in Figure 12 for 0, 10, 20, and 30 wt% of AgNPs content films, respectively. The slopes of linear regions in Figure 12 produce R values given in Table 1.

R values were also plotted in Figure 9 together with B values versus AgNPs content. For the composites with 0 to 10 wt% of AgNPs, R values decrease and then as the weight fraction of AgNPs increased from 10 to 50%, the value of R increases again. From the Figure 9, it is seen that R values show similar behavior as B values produced from fluorescence quenching (lifetimes) data. As was predicted in the previous section, B values or reptation frequency, ν , first decrease as AgNPs content is increased up to 10 wt%, then increases with further increase in AgNPs content. Here, the decrease in R (or ν) values can also be explained by the AgNPs particles merely acted as nanofiller to increase the solvent resistance of the composite films. AgNPs occupy the interstitial space between the PS latexes and act as a barrier for diffusion of solvent molecules and slow down the plasticization effect of solvent molecules for AgNPs content in the range of 0-10 wt%. As a result, PS chains reptate slower at polymer/polymer interface which results in low R and/or B values in these composites. However, the increase in R and/or B values above 10 wt% can be explained by the formation of AgNPs aggregates which causes voids in the films that promote the diffusion of solvent molecules into the films. As a result, as seen in Figure 9, reptation frequency is shown to increase with increasing AgNPs content for these films. Furthermore, it can be seen that highest slope (R) is produced for 50 wt% of AgNPs content film proposing that polymer chains reptate at a higher frequency during film formation process, which result in the largest R-value. This will be explained in detail in the light of SEM images in the next section.

Electrical Properties of PS/AgNPs Composites

The effect of the AgNPs content on the electrical conductivity of PS/AgNPs composite films was also analyzed. The electrical conductivities of film samples were measured by two probe method after the vapor exposure as a function of AgNPs content and the results are shown in Figure 13. The lowest value of conductivity was observed for 1 wt% AgNPs content film.

This deviation may be explained interms of the non-uniform film thickness due to coating method (drop-casting) used in our study. In particular, when increasing the AgNPs content the electrical conductivity of nanocomposites was found to increase from $\sim 10^{-14}$ S for pure PS (0 wt% of AgNPS content) film to $\sim 10^{-11}$ S for pure (100 wt%) AgNPs film. This shows that the conductivity of PS increases by 3 order of magnitude when the AgNPs concentration reaches 100 wt%. This indicates the enhanced conductivity of the PS matrix with increasing AgNPs content. With increasing nanoparticle content, the AgNPs particles form clusters and spacing between them decreases, so that the electron tunnelling between neighbouring clusters and conducting paths through the composite films occur (see Figure 15b, d). This results in an increase in the conductivity of the composite films. However, these conductivity values are typical for insulators

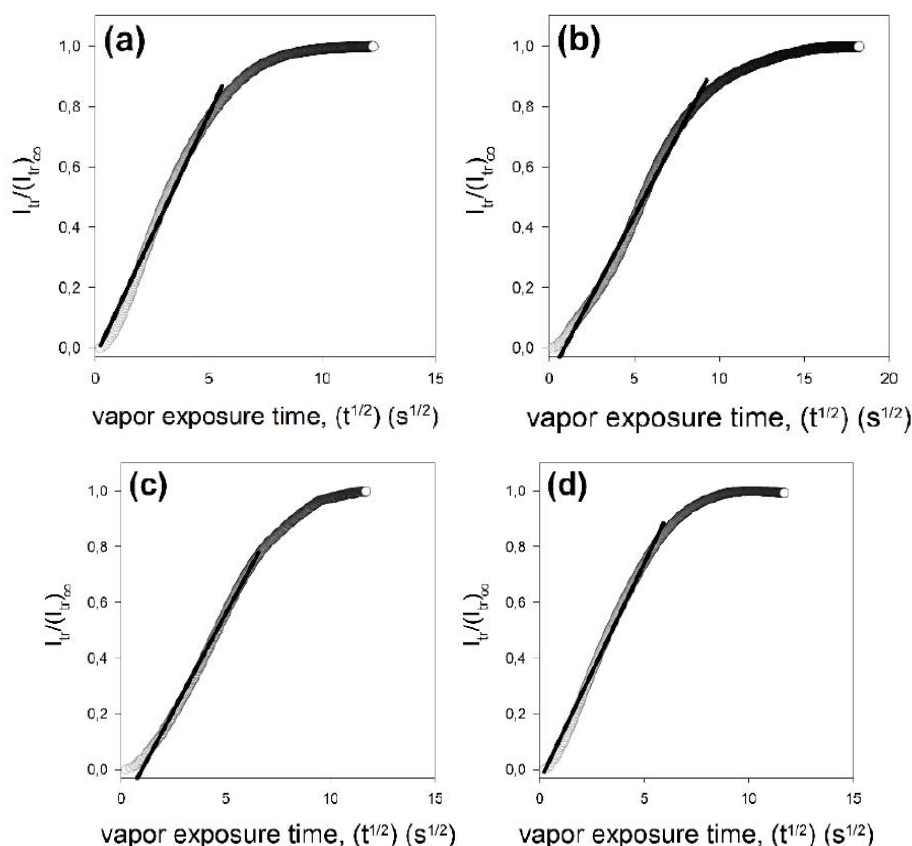


Figure 12: Plot of I_{tr} data in Figure 10 according to Eq. (14) for the (a) 0, (b) 10, (c) 20 and (d) 30 wt% of AgNPs content. The slope of the linear relations produce R values (see Figure 9). R (\square) and B (\bullet) values versus AgNPs content are plotted in Figure 9 together to illustrate the behavior of fluorescence quenching and transparency.

so that the composite films behave like an insulator even at 100 wt% of AgNPs content. Here, it should be noted that the stabilization of silver (Ag) particles by PVP polymer negatively affects electrical conductivity. This is because PVP is an intrinsically insulating stabilizer which puts an insulating layer around the Ag particles so that Ag particles remain

isolated within the polymeric film. So, the possibility of Ag particles to become contacted to form an interconnected conducting pathway is low due to the effective hindrance of the surrounding dielectric PVP. Therefore, no apparent transition zone of a rapid conductivity change is observed for these films at all. The conductivity could be increased further with reducing PVP stabilizer concentration or using a conductive stabilizer.

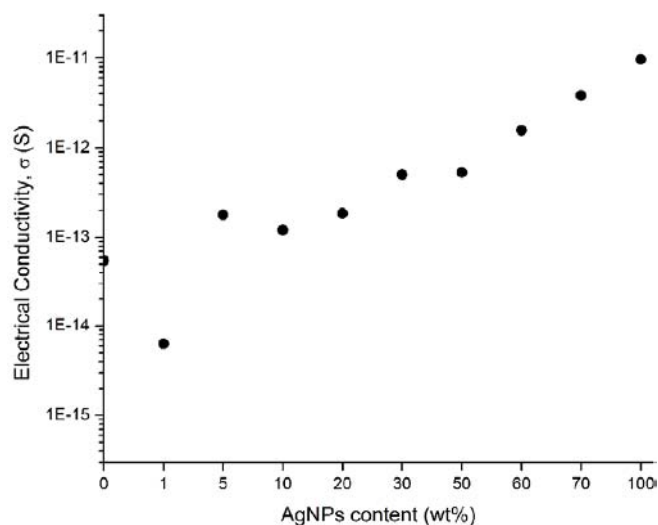


Figure 13: Variation in electrical conductivity, σ (S) of PS/AgNPs nanocomposites with AgNPs content (wt %).

Morphology of PS/AgNPs Composites

In order to support our findings above, SEM was used to examine the morphologies of composites before and after vapor exposure. The images are given in Figures 14 and 15 for the films with 0, 10, 30 and 50wt% of AgNPs content, respectively. Before vapor exposure at $t=0$, for 0, 10 and 30 wt% of AgNPs content films (see Figure 14) the hard PS spheres seem to be randomly distributed and contain a lot of voids, which give lower I_{tr} values at this stage. In addition, some bright spots are clearly visible on the surface and/or between PS latex particles for 10 and 30 wt% content films. Here, the bright spots represent the Ag particles embedded in PVP polymer. The AgNPs occupy the interstitial voids between the PS particles and link them via soft PVP polymer reducing the voids in the 10 wt% of AgNPs content film (inset of Figure 14b). This causes the restriction of PS polymer

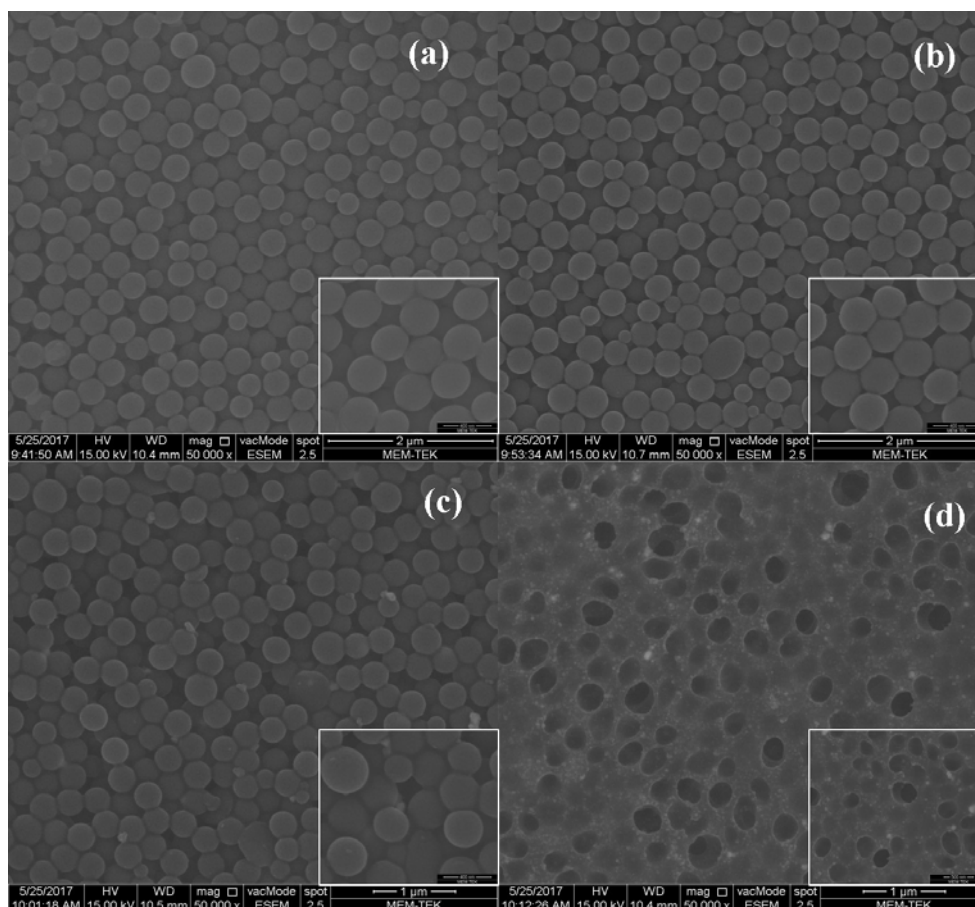


Figure 14: SEM images of PS/AgNPs nanocomposites with (a) 0, (b) 10, (c) 30 and (d) 50 wt% of AgNPs content before exposure of solvent vapor. (Insets show the images taken in higher magnification).

chains during the film formation process exposed to solvent vapor and gives the lowest R and B values for this film (see Figure 9) as stated before.

However, in Figure 14c, PS particles tend to cluster and more voids are observed for 30 wt% of AgNPs content film which presents larger R and B values.

For 50 wt% of AgNPs content film, no PS particles are observed, instead, nearly circular porous surface structure is seen. Here, the influence of low- T_g ($\sim 20^\circ\text{C}$) PVP on the morphology of these composites is expected to be important due to its relatively high concentration. At the highest AgNPs concentration (50 wt%), since 75 wt% of AgNPs is composed of PVP, PVP makes up 37.5 wt% of the composite film. The high fraction of soft PVP polymer was found to affect film formation of PS latex/AgNPs composites, analogous to the film-forming behavior of hard/soft latex blends [47]. Thus, the formation of the circular pores on the surface of 50 wt% of AgNPs content film may be interpreted as follows: When the water in the PS/AgNPs film on glass substrate evaporates, soft (low- T_g) PVP polymer flow and deform concurrently with the evaporation of the water. Coalescence of the soft PVP occurs at the room temperature and form a continuous phase in the composite film with embedded Ag particles in it. However, the hard (high- T_g) PS latexes remain undeformed

after evaporation of water and prevented to come into contact with each other by AgNPs particles. Since they have higher molecular weight ($2.66 \times 10^5 \text{g/mol}$) than PVP polymer (around 3000-4000g/mol), they are buried in soft PVP matrix leaving circular pores at the surface of the composite film. These pores are around 350nm sized as the size of PS particles. Thus, a highly porous film is formed ultimately in this case. This type of structure is responsible for the highest value of R due to the faster diffusion of solvent molecules into the films through these voids which confirms our arguments above.

Figure 15 shows the SEM images of composite films after solvent vapor treatment. It is seen that substantial changes occurred in the morphology of the composite films. The hard PS particles lost their initial spherical shape and formed a more or less continuous phase depending on AgNPs content. The flat and smooth surfaces of all film samples indicate that interdiffusion of the PS polymer chains take place. Despite the flat surface of composite films, AgNPs aggregations are seen with increasing AgNPs content. Here, bright areas in Figure 15b, d are due to the presence of relatively soft AgNPs clusters. Moreover, in the 50 wt% of AgNPs content film, the circular pores are seen to disappear. It is understood that, upon exposure of solvent vapor, the polymer becomes plasticized and sufficiently mobile to self-assemble at the

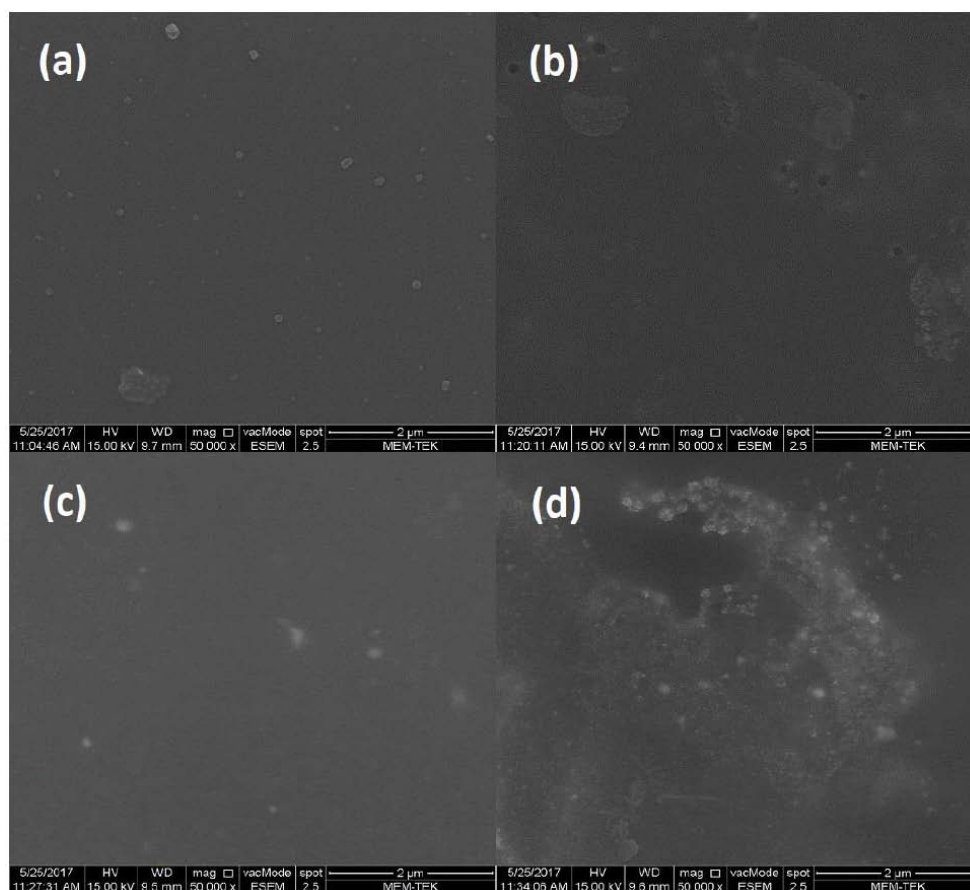


Figure 15: SEM images of PS/AgNPs nanocomposites with (a) 0, (b) 10, (c) 30 and (d) 50 wt% of AgNPs content after exposure of solvent vapor.

room temperature. PS particles come into contact with each other and coalesce forming a continuous network. As AgNPs content increased, AgNPs particles form clusters during the vapor exposure and small clusters are obtained on the surface of 10 wt% of AgNPs content film in Figure 15b. During vapor exposure, the AgNPs clusters grow in size, and form larger clusters with further increase in AgNPs content (see Figure 15c, d). Neighboring clusters meet and touch leading to the percolative AgNPs network which contributes to higher electrical conductivity. The existence of such clusters also explains the decrease in (I_{tr}) values with increasing AgNPs content (see Figure 11) due to the light scattering from the surface of the films. This indicates that chloroform-heptane vapors induce the phase separation of AgNPs and PS polymer, and the interconnected AgNPs clusters can enhance the conductivity of PS/AgNPs films. This observation suggests that this phase separation is induced by the solvent vapor treatment. In conclusion, SEM micrographs confirmed the UVV and fluorescence quenching data and also the increase in conductivity of composites.

CONCLUSION

Powder PS/AgNPs composites with different AgNPs content were prepared by drop casting method at the room temperature. The film formation behavior of these

nanocomposite films exposed to solvent vapor was monitored using fluorescence quenching and photon transmission techniques. The results showed that organic solvent vapor can successfully induce the film formation process of PS/AgNPs composites. The polymer chains obeyed the $t^{1/2}$ law during interdiffusion to form transparent composite films. The SEM images showed a drastic influence of AgNPs content on the structural morphology of the composite films. From these images it was seen that the solvent vapor not only affects the film formation of PS/AgNPs composites but also controls the morphology of the films showing that there is a strong correlation with AgNPs content and vapor-induced film formation of composites, its electrical and morphological properties.

In conclusion, these findings potentially provides a new approach for studying the film formation process of metal doped polymer composites. In addition, we showed that using organic solvent vapor, highly transparent metal-doped composite films (>90%) can be formed. However, only 3 orders of magnitude increase was observed in the conductivity of composite films and films behaved like an insulator even at pure AgNPs film due to the dielectric layer (PVP) surrounding the Ag particles. Reducing dielectric stabilizer concentration or using a conductive stabilizer, the conductivity of composite films could be further increased.

This will be done as future work using the same technique. Various electronic devices that we often used in our daily lives are essentially made up of electrically conductive materials which are also optically transparent in the UV-visible spectrum [48-50]. In this sense, we expect this method to be a practical, facile, and general approach for the fabrication of composite films with high transparency, conductivity and good flexibility.

ACKNOWLEDGEMENT

We would like to thank Prof. Selim Kara for the electrical measurements and Research Assistant Serkan Güçlü for helping us to take SEM micrographs.

FUNDING

This work was financially supported by the Scientific Research Projects (BAP) Unit of Istanbul Technical University (Project number: 40177).

REFERENCES

- [1] Granier V, Sartre A. Ordering and adhesion of latex particles on model inorganic surfaces. *Langmuir* 1995; 11(6): 2179-86. <https://doi.org/10.1021/la00006a054>
- [2] Muller R.-Mall. *Macromol. Symp* 1995; 100: 159-62.
- [3] Wang Y, Winnik MA. Polymer diffusion across interfaces in latex films. *J Phys Chem* 1993; 97(11): 2507-15. <https://doi.org/10.1021/1001113a008>
- [4] Keddie JL, Meredith P, Jones RAL, et al. Kinetics of film formation in acrylic latices studied with multiple-angle-of-incidence ellipsometry and environmental SEM. *Macromolecules* 1995; 28(8): 2673-82. <https://doi.org/10.1021/ma00112a012>
- [5] Mackenzie JK, Shuttleworth RA. Phenomenological theory of sintering. *Proc Phy Soc B* 1949; 62(12): 833-8. <https://doi.org/10.1088/0370-1301/62/12/310>
- [6] Steward PA, Hearn J, Wilkinson, MC. An overview of polymer latex film formation and properties. *Adv Colloid Interface Sci* 2000; 86(3): 195-267. [https://doi.org/10.1016/S0001-8686\(99\)00037-8](https://doi.org/10.1016/S0001-8686(99)00037-8)
- [7] Dragnevski K, Donald A, Taylor P, et al. Latex film formation in the ESEM. *Macromol Symp* 2009; 281: 119-25. <https://doi.org/10.1002/masy.200950716>
- [8] Ludwig I, Schabel W, Kind, et al. Drying and film formation of industrial waterborne latices. *AIChE J* 2007; 53(3): 549-60. <https://doi.org/10.1002/aic.11098>
- [9] Chou TW, Cahn RW, Haasen P, et al. Structure and properties of composites. *Mater Sci Technol* 1993; 13.
- [10] Ugur S, Pekcan Ö. Time evolution of film formation from polystyrene particles: a percolation approach. *Colloid Polym Sci* 2005; 284(3): 1097-1105. <https://doi.org/10.1007/s00396-005-1380-8>
- [11] Colombini D, Ljungberg N, Hassander H, et al. The effect of the polymerization route on the amount of interphase in structured latex particles and their corresponding films. *Polymer* 2005; 46(4): 1295-1308. <https://doi.org/10.1016/j.polymer.2004.11.056>
- [12] Vaessen DM, McCormick AV, Francis LF. Effects of phase separation on stress development in polymeric coatings. *Polymer* 2002; 43(8): 2267-77. [https://doi.org/10.1016/S0032-3861\(02\)00042-3](https://doi.org/10.1016/S0032-3861(02)00042-3)
- [13] Zou H, Wu SS, Shen J. Polymer/silica nanocomposites: preparation, characterization, properties and applications. *Chem Rev* 2008; 108(9): 3893-3957. <https://doi.org/10.1021/cr068035g>
- [14] Schaefer DW, Justice RS. How nano are nanocomposites? *Macromolecules*. 2007; 40(24): 8501-17. <https://doi.org/10.1021/ma070356w>
- [15] Caseri W. Inorganic nanoparticles as optically effective additives for polymers. *Chem Eng Comm* 2009; 196(5): 549-72. <https://doi.org/10.1080/00986440802483954>
- [16] Jurewicz I, Worajittiphon P, King AAK, et al. Locking carbon nanotubes in confined lattice geometries- a route to low percolation in conducting composites. *J Phys Chem B* 2011; 115(20): 6395-6400. <https://doi.org/10.1021/jp111998p>
- [17] Lacour SP, Wagner S, Huang Z, et al. Stretchable gold conductors on elastomeric substrates. *Appl Phys Lett* 2003; 82(15): 2404-6. <https://doi.org/10.1063/1.1565683>
- [18] Roth SV, Santoro G, Risch JFH, et al. Patterned diblock co-polymer thin films as templates for advanced anisotropic metal nanostructures. *ACS Appl Mater Interfaces* 2015; 7(23): 12470-77. <https://doi.org/10.1021/am507727f>
- [19] Rogers JA, Someya T, Huang Y. Materials and mechanics for stretchable electronics. *Science* 2010; 327(5973): 1603-7. <https://doi.org/10.1126/science.1182383>
- [20] Benight SJ, Wang C, Tok JBH, et al. Stretchable and self-healing polymers and devices for electronic skin. *Prog Polym Sci* 2013; 38(12): 1961-77. <https://doi.org/10.1016/j.progpolymsci.2013.08.001>
- [21] Tillman ES, Lewis NS. Mechanism of enhanced sensitivity of linear poly(ethylenimine)- carbon black composite detectors to carboxylic acid vapors. *Sens Actuators B* 2003; 96(1-2): 329-342. [https://doi.org/10.1016/S0925-4005\(03\)00567-7](https://doi.org/10.1016/S0925-4005(03)00567-7)
- [22] Cui J, Daniel D, Grinthal A, et al. Dynamic polymer systems with self-regulated secretion for the control of surface properties and material healing. *Nat Mater* 2015; 14(8): 790-95. <https://doi.org/10.1038/nmat4325>
- [23] Wilson GO, Andersson HM, White SR, et al. Self-healing polymers. *EPST* 2010; 1-33.
- [24] Hsieh H-C, Yang T-J, Lee S. Crack healing in poly (methyl methacrylate) induced by co-solvent of methanol and ethanol. *Polymer* 2001; 42(3): 1227-41. [https://doi.org/10.1016/S0032-3861\(00\)00407-9](https://doi.org/10.1016/S0032-3861(00)00407-9)
- [25] Baek P, Aydemir N, Chaudhary OJ, et al. Polymer electronic composites that heal by solvent vapor. *RSC Adv* 2016; 6(100): 98466-74. <https://doi.org/10.1039/C6RA24296K>
- [26] Birks JB. *Photophysics of aromatic molecules*. New York (NY): Wiley-Interscience 1971.
- [27] Dorrance RC, Hunda TF. Absorption and emission studies of solubilization in micelles. Part 1. -Pyrene in long-chain cationic micelles. *J Chem Soc Faraday Trans* 1972; 68: 1312-21. <https://doi.org/10.1039/f19726801312>
- [28] Cheng S, Thomas JK. Dynamics of pyrene fluorescence in phospholipid dispersions radiat. *Res* 1974; 60(2): 268-79.
- [29] Kalyanasundaram K, Thomas JK. Environmental effects on vibronic band intensities in pyrene monomer fluorescence and their application in studies of micellar systems. *J Am Chem Soc* 1977; 99(7): 2039-44. <https://doi.org/10.1021/ja00449a004>
- [30] Pekcan Ö, Winnik MA, Croucher MD. Direct energy transfer studies on doped and labeled polymer latex particles. *Phys Rev Lett* 1988; 61(5): 641-4. <https://doi.org/10.1103/PhysRevLett.61.641>
- [31] Pekcan Ö, Egan LS, Winnik MA, et al. Fluorescence studies of coalescence and film formation in poly (methyl methacrylate) nonaqueous dispersion particles. *Macromolecules* 1990; 23(10): 2210-6. <https://doi.org/10.1021/ma00210a015>
- [32] Winnik MA, Pekcan Ö, Chen L, et al. Morphology changes and volume deformation of individual phases of polymer blends: fluorescence study of polymer colloids. *Macromolecules* 1988; 21(1): 55-9. <https://doi.org/10.1021/ma00179a013>
- [33] Pekcan Ö. Diffusions and phase relaxations within the interphase domain of polymer blendlike particles. *J Polym Sci* 1996; 59(3): 521-9.
- [34] Crank J. *Mathematics of diffusion 2*. Clarendon (AR): Oxford 1975.
- [35] Birks JB, Christophoron LG. *Proc Roy Soc A* 1963; 274: 552. <https://doi.org/10.1098/rspa.1963.0150>
- [36] Prager S, Tirrell MJ. The healing process at polymer-polymer interfaces. *Chem Phys* 1981; 75(10): 5194-8. <https://doi.org/10.1063/1.441871>
- [37] de Gennes PG. Kinetics of diffusion-controlled processes in dense polymer systems I nonentangled regimes. *J Chem Phys* 1982; 76(6): 3316-22. <https://doi.org/10.1063/1.443328>

- [38] Wool RP, Yuan BL, Mc Garel OJ. Welding of polymer interfaces. *Polym Eng Sci* 1989; 29(19): 1340-67. <https://doi.org/10.1002/pen.760291906>
- [39] Liu YS, Feng J, Winnik MA. Study of polymer diffusion across the interface in latex films through direct energy transfer experiments. *J Chem Phys* 1994; 101(10): 9096-9103. <https://doi.org/10.1063/1.468488>
- [40] Yeo SY, Jeong SH. Preparation and characterization of polypropylene/silver nanocomposite fibers. *Polym Int* 2003; 52(7): 1053-7. <https://doi.org/10.1002/pi.1215>
- [41] Russom A, Gupta AK, Nagrath S, *et al.* Differential interial focusing of particles in curved low-aspect-ratio microchannels. *New J Phys* 2009; 11: 1-11. <https://doi.org/10.1088/1367-2630/11/7/075025>
- [42] Ware WR, James DR, Siemiarczuk A. Stroboscopic optical boxcar technique for the determination of fluorescence lifetimes. *Rev Sci Instrum* 1992; 63: 1710-6. <https://doi.org/10.1063/1.1143328>
- [43] Meeten GH. Optical properties of polymers. London: Elsevier Applied Science Publishers 1986.
- [44] Tzitzinou A, Keddie JL, Geurts JM, *et al.* Film formation of latex blends with biomodal particle size distributions: consideration of particle deformability and continuity of the dispersed phase. *Macromolecules* 2000; 33(7): 2695-2708. <https://doi.org/10.1021/ma991372z>
- [45] Bohn L, Brandup J, Immergut EH. *Polymer Handbook*. 2nd ed. New York: Wiley 1975.
- [46] Rosen SL. Two-phase polymer systems. *Polym Eng Sci* 1967; 7: 115-23. <https://doi.org/10.1002/pen.760070210>
- [47] Ugur S, Sunay S, Pekcan Ö. Film formation of nano-sized hard latex (PS) in soft polymer matrix (PBA): an excimer study. *Polym Compos* 2010; 31(9): 1611-19. <https://doi.org/10.1002/pc.20950>
- [48] Dong SJ, Yan JT, Xu N, Xu J, Wang HY. Molecular Dynamics simulation on surface modification of carbon black with polyvinyl alcohol. *Surf. Sci.* 2010; 605: 868-74. <https://doi.org/10.1016/j.susc.2011.01.021>
- [49] Rozenberg BA, Tenne R. Polymer-assisted fabrication of nanoparticles and nanocomposites. *Prog. Polym. Sci* 2008; 33: 40-112. <https://doi.org/10.1016/j.progpolymsci.2007.07.004>
- [50] Winey KI, Vaia RA. Polymer nanocomposites. *MRS Bull* 2007; 32: 314-22. <https://doi.org/10.1557/mrs2007.229>